Aerosol generation by liquid jet impingement onto a solid surface

Modou Mbaye, Mamadou Sow, Christophe Josserand

▶ **To cite this version:**

Modou Mbaye, Mamadou Sow, Christophe Josserand. Aerosol generation by liquid jet impingement onto a solid surface. Journal of Aerosol Science, 2023, 169, pp.106137. 10.1016/j.jaerosci.2023.106137 . hal-03983946

HAL Id: hal-03983946
https://hal.science/hal-03983946v1

Submitted on 11 Feb 2023

HAL is a multi-disciplinary open access archive for the deposit and dissemination of scientific research documents, whether they are published or not. The documents may come from teaching and research institutions in France or abroad, or from public or private research centers.

L'archive ouverte pluridisciplinaire **HAL**, est destinée au dépôt et à la diffusion de documents scientifiques de niveau recherche, publiés ou non, émanant des établissements d'enseignement et de recherche français ou étrangers, des laboratoires publics ou privés.

Distributed under a Creative Commons Attribution - NonCommercial - NoDerivatives 4.0 International License

Graphical Abstract

Aerosol generation by liquid jet impingement onto a solid surface

Modou Mbaye, Mamadou Sow, Christophe Josserand

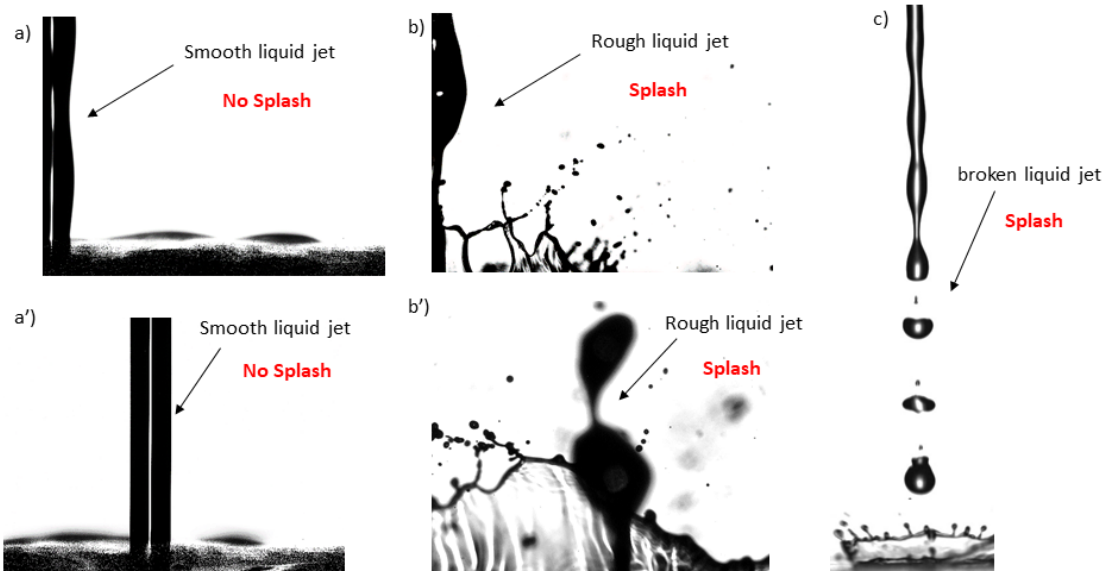

Highlights

Aerosol generation by liquid jet impingement onto a solid surface

Modou Mbaye, Mamadou Sow, Christophe Josserand

- Innovative study on the characterization of aerosolized secondary droplets during a liquid jet impact onto a surface.
- The mass size distribution, the number of aerosolized secondary droplets have been measured and their generation mechanism has been highlighted.
- The airborne release fraction of the aerosolized secondary droplets measured has been fitted with the theoretical splashing parameter.

Aerosol generation by liquid jet impingement onto a solid surface

Modou Mbaye[a,b], Mamadou Sow[a], Christophe Josserand[a]

[a] *Institut de Radioprotection et de Sûreté Nucléaire (IRSN), PSN-RES, SCA, LPMA, Gif-sur-Yvette, 91192, France*

[b] *LadHyX, CNRS & Ecole Polytechnique, UMR 7646, IP Paris, 91128, Palaiseau, France*

Abstract

Liquid jet impinging onto a surface occurs in many industrial process such as nuclear facilities where a part of radioactive material is handled in liquid form. In the case of accidental leak of this liquid, the airborne particle release, in droplets form, is important to quantify since it is the vector of radioactive air contamination. In the literature, while droplets splashing by drop impact have been extensively studied, only few data are available concerning the airborne particle release fraction and the case of liquid jet impact is even less studied. The purpose of this work is to measure aerosol airborne release when a circular liquid jet impacts a solid surface. We found, when the liquid jet is in the Rayleigh regime, so that the jet is broken into multiple drops before impact, the inertia of the impacting drops influences the amplitude of the aerosols mass size distribution but does not change its shape and consequently the aerodynamic mass median diameter. We also show that particle airborne release depends on the impacting Weber and Ohnesorge numbers through the so-called splashing number K which characterizes the splashing transition. We finally propose a quantitative prediction of the aerosol airborne release fraction, valid for $\mathrm{Re} \sim \mathcal{O}(10^3 - 10^4)$ and $\mathrm{We} \sim \mathcal{O}(10^2 - 10^3)$, opening the way to a more general model.

Keywords: liquid jet, splashing, airborne release fraction, secondary droplets

1. Introduction

Liquid fragmentation leading to the formation of droplets aerosols occurs in many natural and technological processes, including diverse phenomena as raindrops splashing on the ground leading to soil erosion or dispersal of spores and micro-organisms, production of sea spray aerosols (SSA), optimizing fuel injection, controlling ink-jet printing quality and enhancing pesticide spray yields in agricultural fileds (Rein, 1993; Yarin, 2006; Josserand and Thoroddsen, 2016; Bergeron et al., 2000). Understanding therefore the formation of aerosols and their transport is crucial for instance to better account for their role in the earth radiation balance (Vignati et al., 2010), the dissemination of pesticides in agricultural fields (Bergeron et al., 2000), the airborne contamination in the form of radionuclides in nuclear facilities (Motzkus et al., 2011) and the spreading of diseases in the air as recently highlighted by the COVID-19 pandemic (Wilson et al., 2020; Balachandar et al., 2020). Generally, droplets aerosol consist of a suspension of liquid particles in the air with a negligible settling velocity, corresponding to droplet diameter typically below $100\,\mu$m (Renoux and Boulaud, 1998). Their residence time in the air vary from seconds to days, depending on their aerodynamic diameter and on the air humidity, so that they can potentially transport hazardous materials on a long-range distance.

In the nuclear industry, some radioactive materials are handled in liquid form. In an accidental scenario such as a liquid leaking, some of the radioactivity can be released into the air in the form of aerosol droplets, as illustrated in figure 1. For instance, airborne resuspension, in particulate form, resulting from the leakage of fission products due to a failed vessel during

spent fuel reprocessing operations has been investigated in the Institute for Radiological Protection and Nuclear Safety (IRSN) by (Motzkus et al., 2009; Sow et al., 2019). The particles of interest are fine enough to penetrate in the human respiratory system and are conventionally classified as inhalable, thoracic and respirable fractions depending on their size, ranging from few tens of microns down to few nanometers (Lindsley et al., 2012).

In the present paper, we investigate in detail experimentally, the droplets aerosols released from the impingement of a circular liquid jet leaking from a container onto a solid surface, in particular in the context of nuclear safety. The goal of the study is chiefly to assess the mass fraction of aerosols generated as well as to identify the secondary droplets formation mechanisms and the droplets size distributions. We intend finally to deduce a quantitative prediction/correlation of this mass fraction, based on a physical modelling using the liquid jet characteristics as well as the precise impact phenomenology (jet breaking regime).

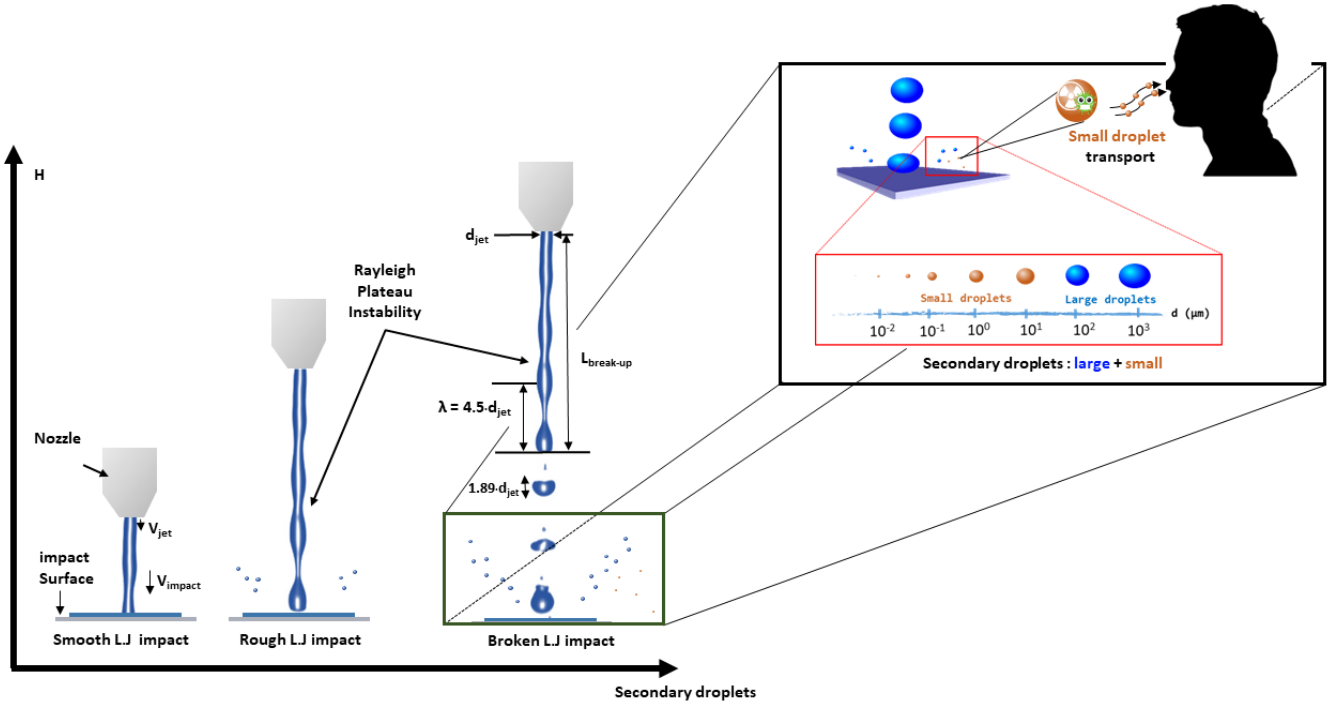

Figure 1: Sketch of splashing mechanism: the increase of the impact height makes instability appear and change the dynamics of the impact which drives in part the airborne contamination. During the splash, zooming zone, several sizes of secondary droplets are generated, small droplets versus large droplets. The small droplets are responsible for air contamination (respirable droplets). The large droplets can contaminate different surfaces.

2. The general problem

We consider a liquid jet delivered out from an air pressurized tank through a nozzle, of diameter d_{jet} at velocity v_{jet} falling from an impact height H on a solid plate, as shown in the schematic figure 1. Depending on the liquid jet parameters and on the fluid properties (impacting liquid and surrounding gas), the liquid jet can impact the plate in different states (Dumouchel, 2008; Eggers and Villermaux, 2008), from a laminar jet at low height, low liquid flux and for viscous liquids, leading to smooth hydraulic jumps (Bohr et al., 1996; Passandideh-Fard et al., 2011), to a turbulent impact where the jet exhibits strong surface deformations, in particular for large jet impinging height H (Lienhard et al., 1992; Wassenberg et al., 2019). Primary drops impact is observed above the so-called breakup length, the distance above which the continuous jet breaks up into primary droplets, because of the Rayleigh-Plateau instability that can develop for large enough H (Leroux et al., 1996). In this latter case, the impact of

the jet is comparable to spray impacts (Breitenbach et al., 2018) and it is often considered as a succession of drop impacts (Roisman et al., 2006). These different configurations are illustrated on figure 2 where experimental images of the jet geometry and impact zone are shown for different jet parameters (section 4: experimental set-up description). We observe on these figures that the production of splashing and thus of small secondary droplets is visible when the jet is strongly perturbed or impacts in the form of multiple drop impacts. These situations appear when the jet instability has enough time to develop before the impact, corresponding to large enough falling height H.

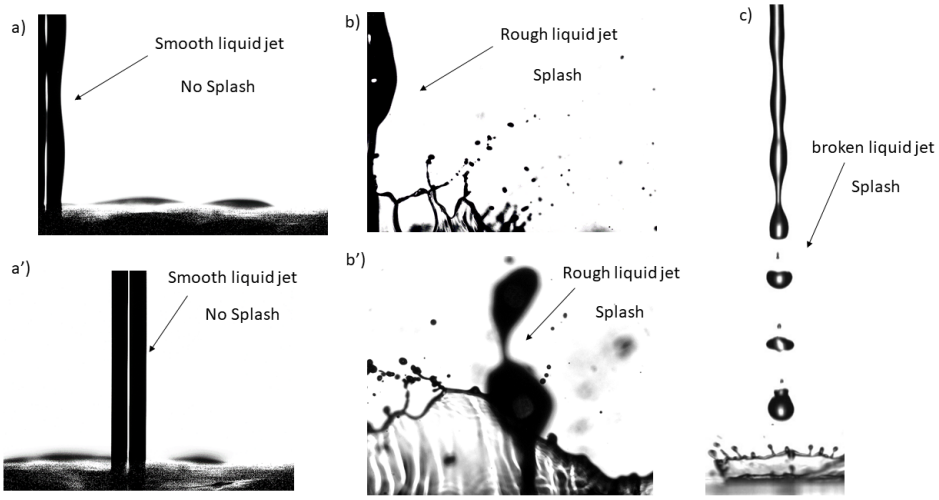

Figure 2: Experimental observations of water jets impacting on the solid plate for different jet parameters. a) and a'), $d_{jet} = 1\ mm$, $v_{jet} = 1.5$ m·s^{-1} and $H_{impact} = 13$ cm, a smooth liquid jet is observed leading to no observable ejected droplets; b) and b'): $d_{jet} = 1$ mm, $v_{jet} = 2$ m·s^{-1} and $H_{impact} = 20$ cm, the jet is strongly perturbed leading to the formation of droplets through the splash of the expanding liquid sheet ; c) $d_{jet} = 2$ mm, $v_{jet} = 2$ m·s^{-1} and $H_{impact} = 30$ cm, the jet is now totally broken into drops that impact irregularly both in space and time on the plate. For the images a) and b), the focusing is done on the jet and, for a') and b'), the focusing is done on 3 mm of the jet.

The goal of our study is thus to characterize and to quantify the aerosol droplets production as a function of the different parameters of the jet. In particular, we will investigate the potential link between the droplets splashed by the impact and the aerosols production. Indeed, in figure 2, secondary smaller droplets are observed, issued either from the corrugated jet or the impact of the primarily drops (due to the break-up of the jet prior the impact). These secondary droplets are apparently generated by the disintegration of the corolla formed by the impact, the so-called corolla splash (Allen and Hughes, 1984; Mundo et al., 1995; Rioboo et al., 2001; Roisman and Tropea, 2002; Josserand and Zaleski, 2003; Josserand et al., 2016). In fact, different mechanisms such as prompt splashes (Thoroddsen et al., 2012; Marcotte et al., 2019) or bubble entrapments (Thoroddsen et al., 2003) can also lead to droplets release. However, they are difficult to identify in the images of figure 2 since they are *a priori* at much smaller scales. This study will thus try, as much as possible, to disentangle the different mechanisms leading to the aerosol production.

Considering the liquid density ρ, its dynamical viscosity μ, the liquid-gas surface tension σ, the liquid jet velocity v_{jet} and liquid jet diameter d_{jet}, the problem depends primarily on three dimensionless numbers, two of which are dynamical. Firstly the Reynolds number:

$$\mathrm{Re}_{jet} = \frac{\rho v_{jet} d_{jet}}{\mu} \tag{1}$$

that quantifies the balance between the jet inertia and the viscous forces; then the Weber number:

$$\mathrm{We}_{jet} = \frac{\rho v_{jet}^2 d_{jet}}{\sigma} \tag{2}$$

which balances inertia and capillary forces. Moreover, the problem depends on the dimensionless falling height:

$$\bar{H} = \frac{H}{d_{jet}}. \tag{3}$$

The Ohnesorge number can also be used instead of one of the two dynamical numbers:

$$Oh = \frac{\mu}{\sqrt{\rho\sigma d_{jet}}} = \frac{\sqrt{\mathrm{We}_{jet}}}{\mathrm{Re}_{jet}} \tag{4}$$

which depends only on the liquid properties and the jet geometry. Although the gas properties (ρ_g and μ_g) involve additional dimensionless numbers, namely the gas-liquid density and viscosity ratios. We do not consider these numbers in our study since we will not vary the surrounding gas (air) in our experiments. To characterize more precisely the impact, it is more relevant to use the impact velocity v_{imp} instead of the initial jet velocity since it is accelerated during its fall, defined by:

$$v_{imp} = \sqrt{v_{jet}^2 + 2gH} \tag{5}$$

where g is the gravity. This theoretical velocity is deduced considering at first approximation the free fall of the jet and this formula has been verified experimentally. In addition, due to the capillary forces, when the jet breaks, the formed drops have a diameter d_{imp} larger than the diameter of the liquid jet. From the Rayleigh-Plateau instability, we estimate the drop diameter as (Dumouchel, 2008):

$$d_{imp} = 1.89\, d_{jet}. \tag{6}$$

Using the impact velocity and the impact diameter, we obtain the two corresponding dynamical dimensionless numbers for the impact:

$$\mathrm{Re}_{imp} = \frac{\rho v_{imp} d_{imp}}{\mu} \quad \text{and} \quad \mathrm{We}_{imp} = \frac{\rho v_{imp}^2 d_{imp}}{\sigma}, \tag{7}$$

the impact Ohnesorge number is adjusted accordingly:

$$Oh_{imp} = \frac{\sqrt{\mathrm{We}_{imp}}}{\mathrm{Re}_{imp}} = \frac{\mu}{\sqrt{\rho\sigma d_{imp}}} \tag{8}$$

Finally, we can emphasize that for high impact heights, when the jet breaks up into drops, different configurations can be encountered as illustrated on figure 3. When the impact height is very large compared to the break up length of the jet, the distance crossed by the drops before the impact becomes important, which favors successive and simultaneous drops impact. Our study will in fact cover these different impact configurations.

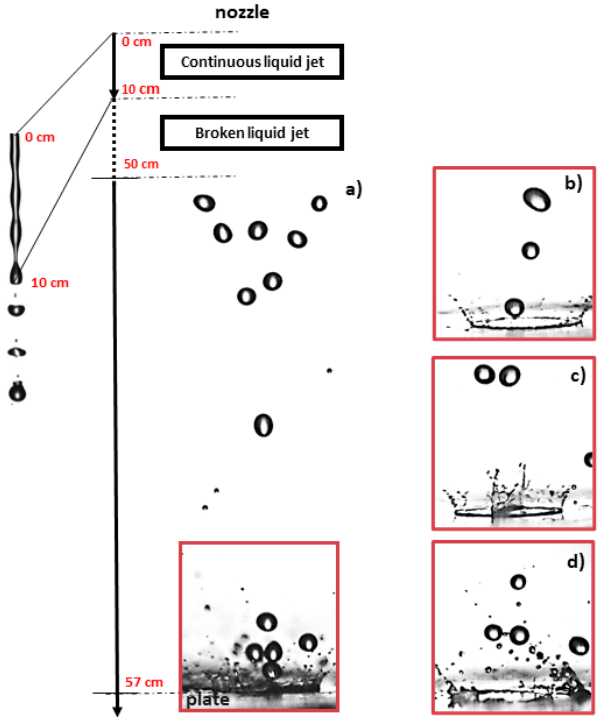

Figure 3: Illustration of different drop impact configurations . This illustration was done with a 1 mm liquid jet diameter ejected from the nozzle at 2 $m{\cdot}s^{-1}$. The breakup length of the jet is around 10 cm and the impact height (nozzle-plate distance) is fixed at 57 cm. a) combination of different drops impact, b) successive drops impacts, c) simultaneous drops impacts with crown splash interaction and d) successive and simultaneous drops impacts.

3. Secondary droplets and aerosols

When the jet has broken into primary droplets, we are facing the impact of drops whose radius is of millimeter size. These impacts lead to the formation of much smaller secondary droplets which are those of interest for aerosol dissemination (Thoroddsen et al., 2012). The emitted droplets are subject both to gravity and to the surrounding airflow so that the aerosolized droplets are those for which the air entrainment can balance their weight. Indeed, for nuclear contamination, we are interested in droplets and droplet nuclei in the breathable size range containing radioactivity which can remain suspended in the air, and hence can be airborne vehicles of radioactive contamination. In terms of air contamination, the droplets more than 100 μm have usually a ballistic trajectory and will settle quickly. They are in general considered not to contribute widely to the air contamination although they might be crucial in surface contamination (Bourouiba, 2021). Therefore, in our study, we will not focus on the droplets produced by the drop impacts with a radius larger than 100 μm, which are called hereinafter large secondary droplets, and which have been studied in details in the literature (Allen and Hughes, 1984; Mundo et al., 1995; Rioboo et al., 2001; Roisman et al., 2006; Josserand and Zaleski, 2003; Josserand et al., 2016; Okawa et al., 2022).

It is however crucial to estimate below which radius the droplets can remain as a suspension in the flow and thus transform into aerosols. The size of secondary droplets produced by millimetric liquid impact is typically ranging from $\mathcal{O}\,(1\,\mu m)$ and $\mathcal{O}\,(1\,mm)$, leading to a large range of settling velocities, as plotted on figure 4 using the classical relation due to the balance between gravity and drag taken from (Renoux and Boulaud, 1998). Thus, one can easily estimate the critical size of the particles/droplets remaining suspended by balancing the settling velocity with the surrounding air typical velocity.

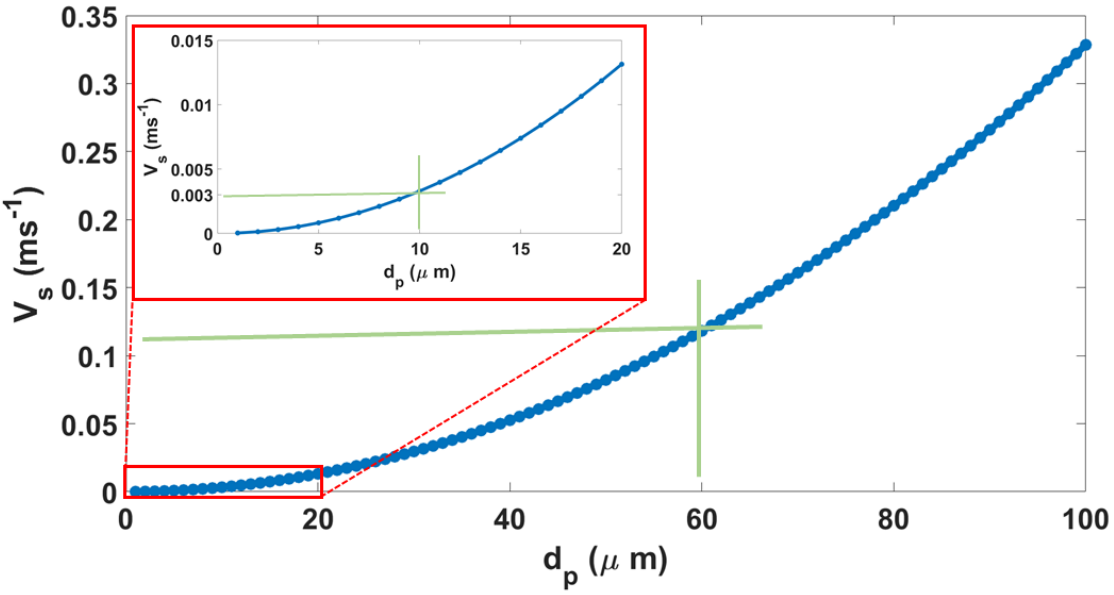

Figure 4: Falling terminal velocity of water droplets as a function of the droplet diameters. The inset Figure is a zoom on the terminal settling velocity curve for aerosols droplets between 0 and 20 μm.

4. Experimental set-up

To quantify and characterize the aerosols generated by a liquid jet impingement, we designed an experimental device named DICAPRIO (DevIce for the ChAracterisation of Particle Resuspensed by liquid jet Impingement and their Observation). The device consists of a $0.84 \times 0.74 \times 1.00$ m closed box of inside volume $V_e = 0.62$ m^3 from which a liquid jet is released from an air pressurized tank through a nozzle at a certain height above the plate. A schematic diagram of the experimental set up is shown in figure 5. The structure of the device is made of aluminium profiles and the walls are made of Plexiglas. The connection between the profiles and the walls is made with sealing gaskets. The temperature and relative humidity inside the device are measured with a vwr probe (reference 620-2273, ± 0.1 $°C$, ± 0.2 %). The impact height of the jet is controlled by a graduated sliding link attached to the impact surface made of stainless steel.

The ventilation and the sampling points in the experimental enclosure have been specifically designed to guarantee a sampling representativeness of the aerosols produced during the impingement of a liquid jet. The aerosols are quantified by sampling at a constant flow rate, high enough to collect small airborne particles produced by the splashing of the primary drops. In addition, the homogeneity of the air mixing in the enclosure has been successfully verified through gas tracing and numerical simulations (using RANS k-omega model with Ansys Fluent® code). The main results are the following: for an air flow rate of $Q_{ext} = 275$ L·min^{-1} the experimental air exchange time (time needed to extract 63% of the air containing aerosols inside of the enclosure) is equal to 2 *minutes and* 20 *seconds*. This value matches with the theoretical exchange time $t_r = V_e/Q_{ext} = 620/275 = 2$ minutes and 15 seconds. The numerical simulations show that the local air velocities inside of the experimental enclosure remain below 0.5 m·s^{-1}, which is associated with vertical velocity fluctuations of the order of $0.05\,\mathrm{m \cdot s^{-1}}$. Thus, the airflow around the particles can be considered as laminar and the approximation of aerosol sampling in steady air conditions can be made accordingly. Moreover, comparing

the purification time of the experimental enclosure (which depend on the airflow sampling rate and its empty volume) to the settling time of the particles (that is size dependent) we can approximate that most of the emitted droplets below 25 μm are correctly sampled. The results on the particle size distribution presented in section 5.3 are in agreement with this reasoning. In particular, the initiation of a mode in a size range around 25 μm has not been observed.

We performed a gas tracing with helium (data not shown), and we observed a single exponential decrease of the helium concentration when the injection was stopped. This behavior during the enclosure purification phase is representative of a homogeneous air mixing according to the ventilation theory (Baron and Willeke, 2001). Moreover, the same behavior is noticed during the aerosol purification phase, following the end of the liquid impact, as recorded with the APS particle counter with a single exponential decay of concentration. Therefore, there is no dead zone (zone without good air mixing) in the enclosure, which suggest a very homogeneous concentration of aerosols in the enclosure.

The impinging liquid is stored in a pressurized tank to control the injection velocity of the jet. The over-pressure imposed in the tank is measured with a manometer and adjusted with a valve in the range between 0 and 1 bar in steps of 0.1 bar. For all the experiments, we have used the same volume of liquid of 2.5 L (liter) of demineralized water with 199 g·L^{-1} of NaCl, and 0.4 g·L^{-1} of sodium fluorescein. The latter is the non-radioactive surrogate used for contamination, while the former is utilized to increase the limit of detection of aerosols for the measuring instruments.The surface tension and the dynamic viscosity of the impacting liquid have been measured with a Noüy ring tensiometer (model Kruss BP2) and rolling-ball viscometer (model Lovis 2000 M/ME), respectively.The liquid temperature is controlled by a heating rod inside the tank regulated at 20 $°C$. The flow rate of the outgoing liquid is measured with an electromagnetic flow meter in the range of 0.12 - 1 L·min^{-1}. A programmable electromagnetic valve is placed upstream of the nozzle.

In order to minimize turbulence at the nozzle outlet and to have a stable jet, we designed a convergent nozzle with a convergence angle of 30°, a contraction ratio of 11 and a aspect ratio of 20. Three nozzles of 1, 1.5 *and* 2 *mm* diameter are used and the jet velocity varied in our experiments from 1 to 6 m·s^{-1}. Finally, the impact velocity has been measured experimentally and has been found in good agreement with equation 5 with an error of ±5%.

Our experimental strategy is developed around the measurement of the S_{ARF} (Splashing Airborne Release Fraction which is proportional to the total mass of produced aerosols), the measurement of the size distribution of aerosols and the observation of the mechanism of their formation.

4.1. Airborne release fraction measurement

Soda fluorescein is used in our experiments as a surrogate contaminant material that is dissolved in the impacting liquid. It is a very suitable airborne resuspension tracer thanks to its very high specificity and its very low limit of detection down to 100 ng·L^{-1} in solution. The total mass of aerosols produced during the impingement , $m_{aerosol}$, is collected by aspiration on a filter by circulating inside the enclosure clean and dry air through 3 ports equipped with a very high efficiency filter (figure 5 left) with an extraction flow rate of 275 L·min^{-1}. The inlet ports are purposely placed to ensure a homogeneous aerosol mixture inside.Thus, at the outlet of the aspiration, figure 5 right, the aerosol-laden air passed through a filter. The filter loaded of aerosols is dipped in water at slightly basic pH to maintain fluorescence properties of the tracer and the washing solution analyzed by a spectrofluorometer ESElog Fluorescence Detector (the mass of the aerosols is too small to consider weighing the filter).

From the mass of collected aerosols, we defined the splashing airborne release fraction (S_{ARF}) as the ratio between the mass of aerosols collected m_a (mass of fluorescein collected) and the total mass of fluorescein injected (dispersable mass) m_i:

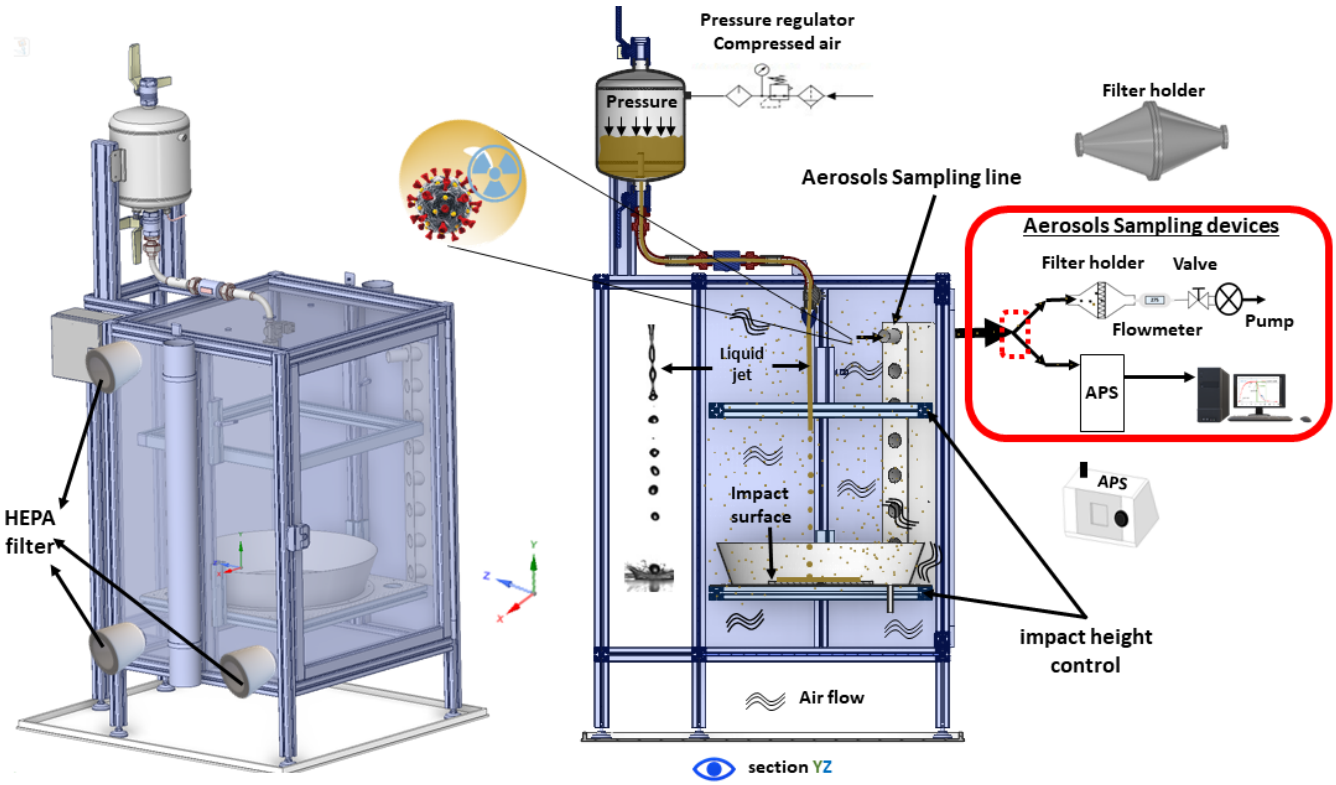

Figure 5: 3D schematic overview of experimental apparatus (left), section view of aerosols sampling techniques (Right).

$$S_{ARF} = \frac{m_a}{m_i} \tag{9}$$

The study of the generation of aerosols from the leakage of hazardous material and single drops impact onto a surface realized at IRSN by (Motzkus et al., 2009) and (Sow et al., 2019) shows that splashing airborne release fraction is in the range of $\mathcal{O}(10^{-6} - 10^{-5})$.

4.2. Size and mass distribution

For the airborne size and mass distribution, the aerosol-laden air is directed toward a 2 cm diameter sharp-edged nozzle connected to an antistatic tube of 15 cm of long. The tube is connected to an Aerodynamic Particle sizer (APS, TSI model 3321). The APS spectrometer measures aerodynamic diameter by light-scattering intensity. The device provides accurate count size distributions for particles with aerodynamic diameter d_{ae} in the size range $0.5 < d_{ae}(\mu m) < 20$. Light scattered by the particles passing through two successive laser beams is collected by a photodetector that converts the light signal into an electrical signal whose shape pulse determines the aerodynamic particle size with time-of-flight (TOF) method. Its low sampling rate of 5 L·min^{-1} allows the monitoring of the total particle concentration and size distribution without altering the aerosol concentration produced by the impact of the jet inside of the enclosure. Finally, one can rely the aerodynamic diameter d_{ae} to the effective diameter of the aerosols droplets, d_{sf}, which is the diameter of a spherical particle with the same density and settling velocity as the particle of interest, through the relation:

$$d_{sf} = \left(\frac{\rho_0}{\rho_p}\right)^{\frac{1}{2}} \times d_{ae}, \tag{10}$$

where ρ_0 et ρ_p are the density of a spherical water droplet and a particle of interest.

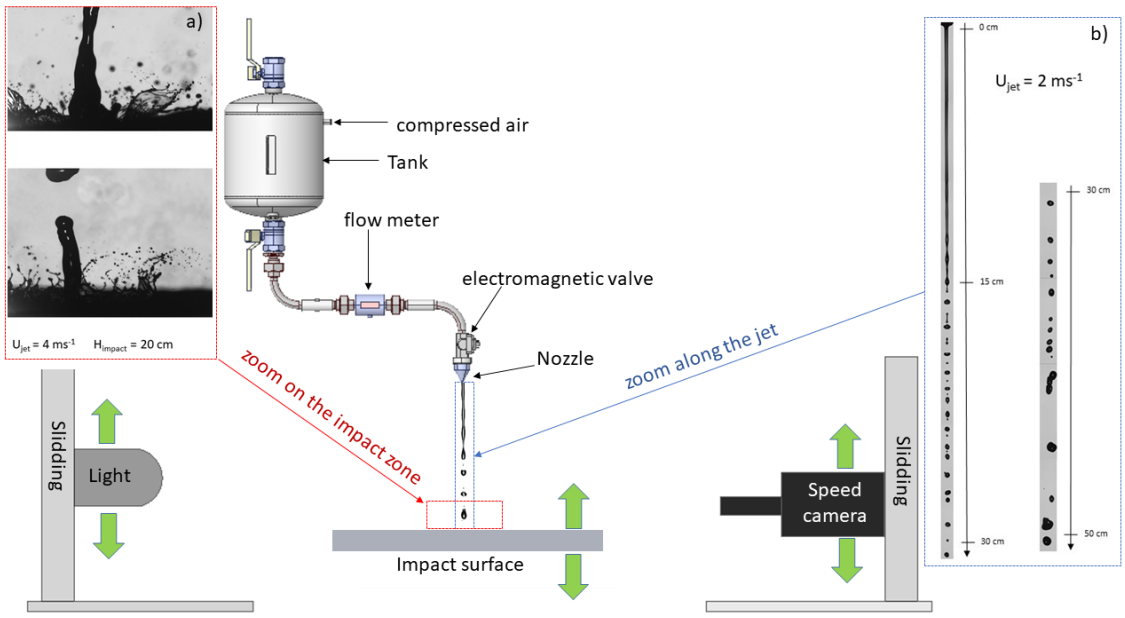

Figure 6: Imaging setup. We used backlight imaging of the impacting liquid and along the jet. a) Field of view of the impact area to identify the mechanisms behind the production of large secondary droplets and aerosolized secondary droplets. b) Observation along the jet to characterize the break up length of the jet, to determine the impact velocity and also the impact frequency.

4.3. Experimental protocol

To keep the enclosure as clean as possible between each test, its walls are completely covered with an antistatic sticky film that is replaced after each test. This step can take 45 minutes. The protection phase is followed by a 30 minutes noise measurement phase where almost all the aerosols impurities present in the enclose are purified at a flow rate of 275 L·min^{-1}. This flow rate corresponds to the sum of the flow rate of the external pump which makes it possible to collected the totality of the aerosols on filter, 270 L·min^{-1}, and the flow rate of the APS 5 L·min^{-1}. This noise measurements provides the background noise of the tests. After changing the filter in the blank experiment, we impact the liquid jet on the impact plate. Since all our tests were performed with a equivalent volume of 2.5 L of solution, the duration of the impact depends on the flow rate of the liquid jet. This time can vary between 2.5 and 20 minutes. During 30 minutes after the end of the jet impact, the aerosol produced are collected on the filter at 270 L·min^{-1} and sampled with the APS at 5 L·min^{-1}.

4.3.1. Liquid visualisation

Since the enclosure does not allow an accurate vizualisation of the liquid jet from the nozzle to the plate, a second experimental set-up has been designed outside the box, as shown on figure 6. The mechanisms in the pre-impact and impact zone are visualized with a Dantec camera using a laser illumination. With this device, the spatial resolution is 2344 x 2545 pixels. For a working field of 5 cm the resolution is thus 21 x 20 $\mu m/px$. Thanks to its double pulse character, this camera provides a good temporal resolution of 1.2 ms.

This device also allows us to determine the impact velocities of the jet as well as those of the primary drops resulting from the rupture of the liquid jet. The mechanisms in the post-impact zone with the characterization of smaller secondary droplet size, are analysed with a high resolution camera (Baumer, LXG-500C) of full frame, 7920 x 6004, with a maximum of 5 fps. For a working field of 1 cm, the resolution is thus 1.2 x 1.6 $\mu m/pixel$

5. Results and discussion

In this section, we will present two main types of results. On the one hand, using a liquid composed of 50% water and 50% glycerol with a concentration of fluorescein of 0.4 $g.L^{-1}$, we will illustrate the fact that the shape of the impacting liquid has a strong influence on the aerosols produced, on the other hand, using demineralized water with NaCl and fluorescein with a concentration of 199 $g.L^{-1}$ and 0.4 $g.L^{-1}$ respectively, we will show the influence of the velocity and diameter of the impacting drop. At the end, we propose a formula for the prediction of the mass fraction of aerosols in suspension and we will show the origin of these aerosol droplets by imaging.

5.1. Influence of the jet geometry at impact

To evaluate the influence of liquid jet geometry, a liquid consisting of a mixture of 50% water and 50% glycerol with soda fluorescein was used. As illustrated above on figure 2, the impact of the liquid jet exhibits different features as the falling height H varies, from (almost) smooth jets at small H, to corrugated jets and even train drops impacts as H increases. We will firstly demonstrate that this geometrical structure of the jet plays a crucial role in the aerosol production. In that purpose, we show on figure 7 the evolution of the mass fraction of aerosolized secondary droplets S_{arf} as a function of the impact velocity for jets of the same liquid with the same nozzle diameter d but with three different initial jet velocities and different falling heights. Similar impact velocities can thus be reached for different initial jet velocities: for instance $V_{impact} = 4$ m·s^{-1} can be reached both for $v_{jet} = 1.8$ m·s^{-1} with $H = 57$ cm and for $v_{jet} = 3.5$ m·s^{-1} with $H = 20$ cm. Although these two configurations have the same dynamical parameters (Re_{imp} and We_{imp}), we observe surprisingly that for the smaller $H = 20$ cm, S_{arf} is of the order of the measurement noise (indicated by the red line), while it is much higher for $H = 57$ cm. In fact, it is clear from the figure 7, that the higher the falling height H, the higher the S_{arf} for the same impact velocity. The snapshots of the impacting jets shown on the same figure near each experimental dots exhibit that no aerosolized secondary droplets are produced when the jet is not broken at impact. Such behaviour has been observed by (Errico, 1986; Lienhard et al., 1992; Trainer, 2016; Zhan et al., 2020). These results indicate that the impacting velocity and thus the dynamical parameters cannot be the single parameters characterizing the aerosol production and that the jet geometry at impact is crucial.

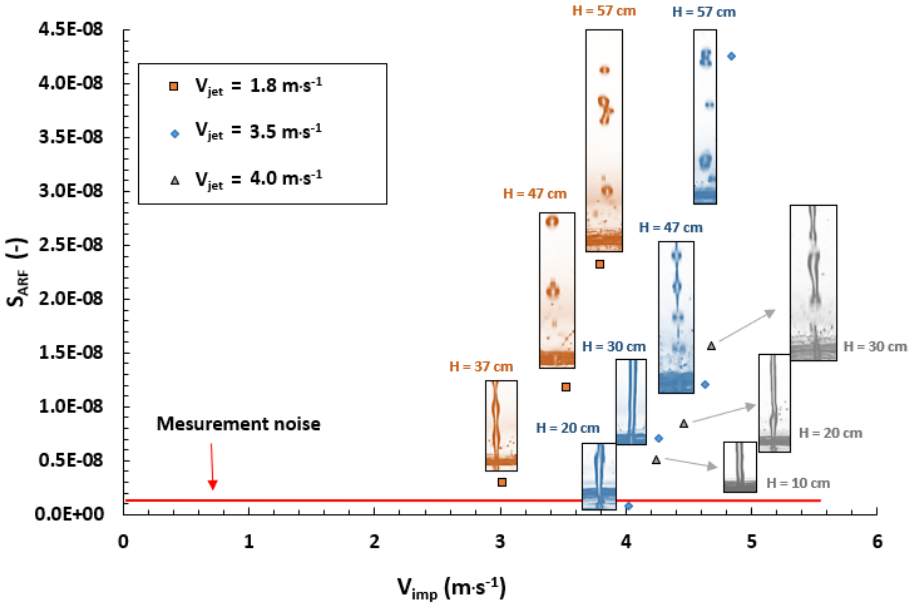

Figure 7: The aerosol released fraction S_{arf} as a function of the impact velocity v_{imp} for different initial jet velocities v_{jet}, as indicated in the inset of the figure, using three different colors (orange, blue and gray) for the jet velocities $v_{jet} = 1.8\ m{\cdot}\mathrm{s}^{-1}$, $v_{jet} = 3.5\ m{\cdot}\mathrm{s}^{-1}$ and $v_{jet} = 4.0\ m{\cdot}\mathrm{s}^{-1}$ respectively. The liquid jet is released from a nozzle of diameter $d = 2\ mm$ with a solution composed of 50% of water and 50% of glycerol (with a surface tension and viscosity equal to $\sigma = 0.066\ \mathrm{kg}{\cdot}s^{-2}$ and $\mu = 0.005\ \mathrm{kg}{\cdot}s$ respectively) from different falling height H. The snapshot of the jet at impact is shown for each point of the figure, labelled by the falling height H. The square, diamond and the upward-pointing triangle symbol correspond to velocities $v_{jet} = 1.8\ \mathrm{m{\cdot}s}^{-1}$, $v_{jet} = 3.5\ \mathrm{m{\cdot}s}^{-1}$ and $v_{jet} = 4.\ \mathrm{m{\cdot}s}^{-1}$ respectively.

Indeed, the visualisations of the impacted region for these three configurations, shown on the same figure 8, suggest that the aerosol production is directly linked to the corolla splashes that are present in the case of the corrugated jets and droplet impacts. In fact, by varying the jet thickness and velocity, and the falling height, we have only observed detectable S_{arf} (defined as at least ten times the apparatus noise signal) when corolla splashes were present, demonstrating that the aerosol production in these experiments are clearly due to the disintegration of the corolla formed by the splashing of the corrugated jet or the drops train.

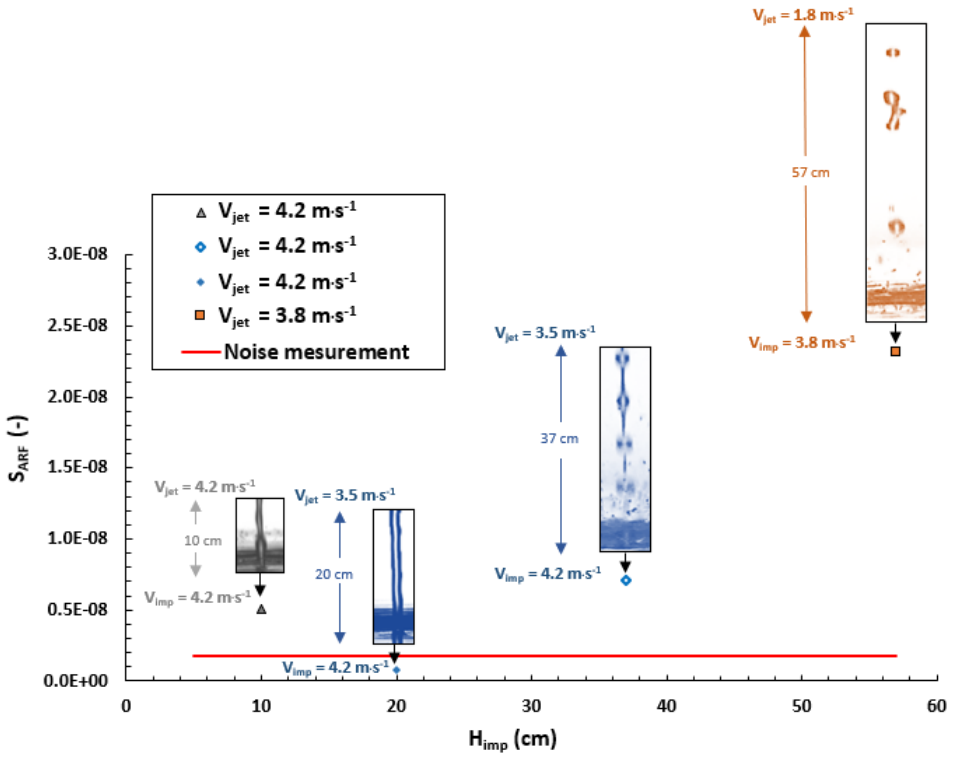

Figure 8: The aerosol released fraction S_{arf} as a function of the impact height H_{imp} for four different liquid jets but with the same impact velocity, v_{imp}, as indicated in the inset of the figure, using four different colors (orange, gray, yellow and green) for a turbulent, a laminar, a pseudo broken and a totally broken liquid jet. The liquid jet is released from a nozzle of diameter $d = 2\ mm$ with a solution composed of 50% of water and 50% of glycerol (with a surface tension and viscosity equal to $\sigma = 0.066$ N$\cdot m^{-1}$ and $\mu = 0.005$ Pa$\cdot s$ respectively) from different jet velocity V_{jet}. The snapshot of the jet at impact is shown for each point of the figure, labelled by the jet velocity V_{jet}.

Although the transitions between these three impact regimes and the evolution of the aerosolized secondary droplets production with the impact parameters for the continuous and corrugated liquid jet cases are of great interest, we will focus in the following our study on the train drops impact only since it is the most favorable situation for aerosol production. We postpone then the detailed analysis of the influence of the jet geometry on the aerosols production to further studies.

5.2. The splashing airborne release fraction of aerosolized secondary droplets : S_{ARF}

To evaluate the influence of liquid jet diameter and the impact velocity, presented hereinafter, a liquid consisting of a mixture of demineralized water with NaCl and fluorescein was used. All results presented from now correspond to the parameters listed on table 1. The Weber, Ohnesorge and Reynolds numbers of the impact correspond to a 1, 1.5 and 2 mm liquid jet diameter and impacting velocity between 3.5 and 7 m$\cdot$s^{-1}. The physico-chemical properties of the solution used in terms of surface tension, viscosity and density are: $\sigma_g = 0.068$ kg$\cdot$s^{-2}; $\mu = 0.0011$ kg$\cdot$ m$^{-1}\cdot$s^{-1} and $\rho = 1115$ kg$\cdot$m^{-3} respectively.

Table 1: Variation ranges of the dimensionless parameter for the three jet thickness d_{jet} = 1, 1.5 and 2 mm from top to bottom.

$Re_{imp} \times 10^3$	$Oh_{imp} \times 10^{-3}$	$We_{imp} \times 10^2$
11.01 - 19.88	2.30	6.39 - 20.85
12.01 - 23.38	2.15	6.71 - 25.45
10.32 - 20.92	2.00	5.62 - 17.50

We now investigate how the fraction of aerosolized secondary released droplets S_{arf} evolves as we vary the jet velocity and thickness for our liquids with a constant falling height $H_{imp} = 57$ cm such that at impact the jets have broken into pieces and are always formed by irregular drops impacts. Figure 9 shows S_{arf} as a function of the impacting velocity v_{imp} for the three different investigated jet diameters $d_{jet} = 1$ mm (top), $d_{jet} = 1.5$ mm (middle) and $d_{jet} = 2$ mm (bottom). We observe clearly that the aerosol fraction released by the impingement of the liquid jet increases with the impact velocity v_{imp}.

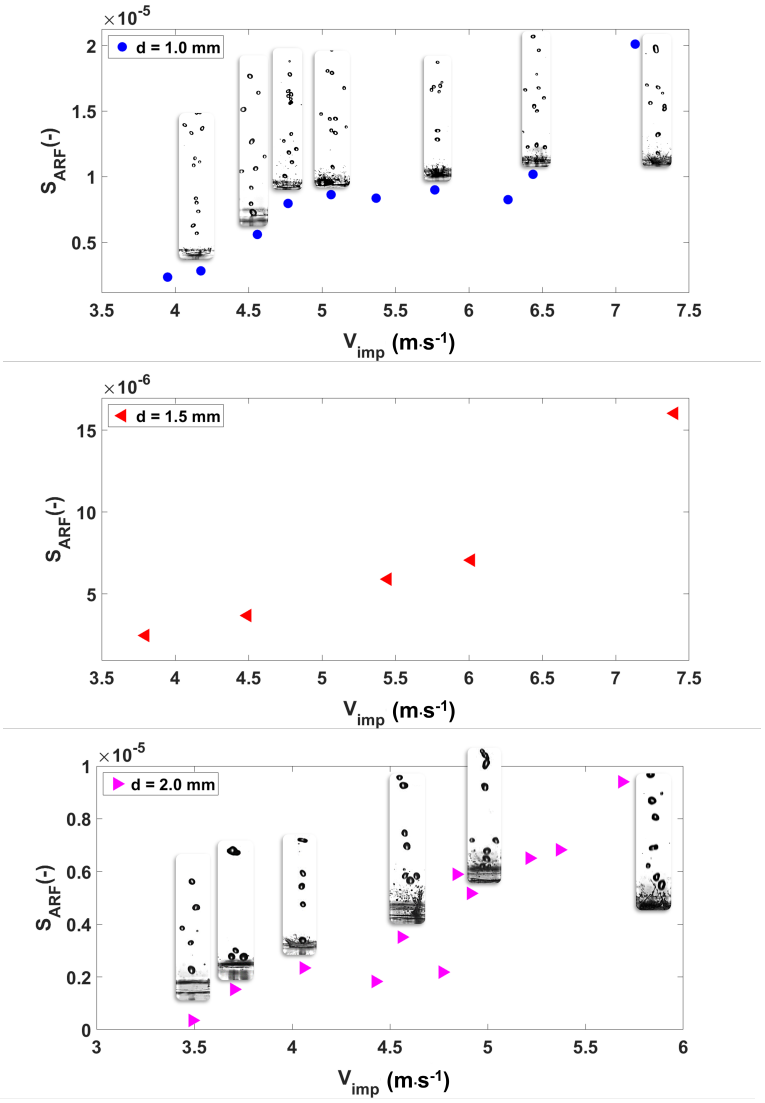

Figure 9: Splashing airborne release fraction as a function of the liquid jet impact velocity for : top) d = 1 mm ; middle) d = 1.5 mm and bottom) d = 2 mm. The impact height is fixed at 57 cm. The insert image on each point of the figure illustrate the dynamic of the impact : successive, simultaneous or successive and simultaneous impact.

Following previous references on aerosol production (Okawa et al., 2006; Motzkus et al., 2011; Sow et al., 2019), we plot the S_{ARF} as a function of the Weber number, as shown on figure 10, for the different nozzle diameter associated to different Ohnesorge number. While the curve shows that the competition between inertia and capillarity, quantified by the Weber number, is crucial for the aerosol production, it is not enough since it varies with the nozzle diameter. This indicates that another dimensionless number related to the impact is involved, either the Reynolds or the Ohnesorge numbers, which implies that viscous effects play a role in the dynamics.

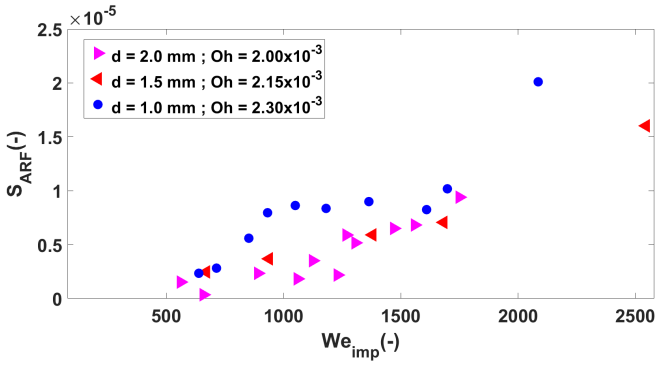

Figure 10: Splashing airborne release fraction as a function of the impact Weber number for a small variation of the Ohnesorge number. The symbols right-pointing triangle, left-pointing triangle and circle correspond to liquid jet of diameter 2 mm, 1.5 and 1 mm respectively.

In fact, as illustrated by the vizualisations of the impacts, it is tempting to associate the aerosolized secondary droplets production with the quantity of liquid splashed by the impact. In the literature, many formula have been proposed to predict primarily the splashing transition but also sometimes the mass ratio between the secondary droplets emitted by impact with the impacting droplets (Moreira et al., 2010). Considering that the splashing is mostly due to the interaction between inertia, capillarity and viscous effects, a splashing parameter K is usually introduced, using dimensional analysis, which can be written in a general form as:

$$K = Oh^a We^b \tag{11}$$

where the exponents a and b vary according to the models ($-0.4 < a < 0.4$ and $-0.3 < b < 1$) depending whether the impacted surface is dry or wet, the latter corresponding to the present situation since our drops impact on the thin liquid film formed by the impacts of the preceding droplets. The splashing transition is then characterized by a critical value of the parameter K_c, deduced either from experiments or by modelling, below which the drop simply spreads smoothly after the impact and above which splashes appear. Such splashing parameter has been firstly introduced as an experimental correlation by (Stow and Hadfield, 1981), followed by others works, using theoretical, experimental and numerical approaches (see for instance (Wu, 1992; Bai and Gosman, 1995; Mundo et al., 1995; Yarin and Weiss, 1995; Josserand and Zaleski, 2003; Vander Wal et al., 2006)). Among the different proposed formula, we would like to highlight one that is deduced from the modelling of the flow lamella produced by the impact which has shown good agreement with experiments

$$K = Oh^{-0.4} We \tag{12}$$

Although the link between the splashing parameter and the mass fraction of droplet splashed above K_c is not straightforward (Roisman et al., 2006; Moreira et al., 2010), it seems natural to expect that this ratio is also depending on the splashing parameter, with the splashing airborne ratio being zero below $K < K_c$ and increasing above $K > K_c$. For instance, (Okawa et al.,

2006) has proposed an empirical correlation for the number of large secondary droplets N_{lsd} produced during drop impacting (allowing then the computation of the splashed mass ratio) as a function of the splashing parameter K highlighted above, eq. (12), following

$$N_{lsd} = 7.84 \times 10^{-6}(K)^{1.8} H^{-0.3}. \tag{13}$$

In fact, this correlation is better suited for impacts onto thin liquid films, satisfying $H = h_{film}/D_{drop} < 2$ [1].

Finally, we cannot *a priori* rely directly the aerosol released fraction to the splashed mass: in particular, we observe that the larger secondary droplet simply fall on the liquid film without producing aerosols. However, it is reasonable to question whether the aerosol released fraction (airborne tiny aerosols droplets) is *actually* a function of the splashing parameter. In that purpose, figure 11 illustrated the evolution of the splashing airborne released fraction S_{ARF} as a function of the impact splashing parameter $K = \mathrm{We}_{imp}\mathrm{Oh}^{-0.4}$.

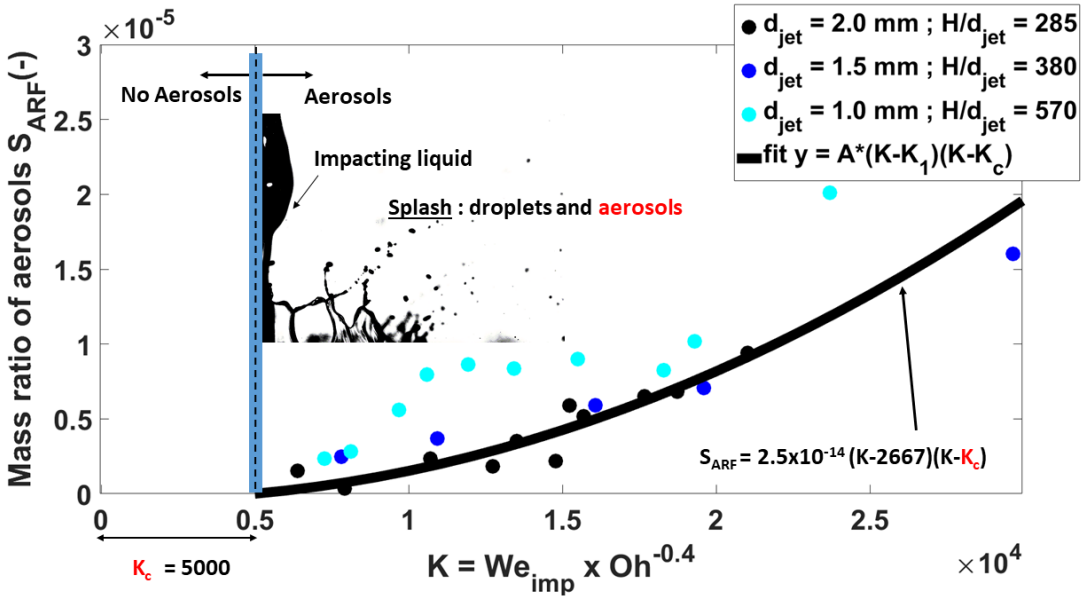

Figure 11: Splashing airborne release fraction as a function of the splashing number based on the Weber and Ohnesorge number of impact for three liquid jet diameter 1 mm, 1.5 mm and 2 mm corresponding to the cyan, blue and black color. The impact height H is fixed to 57 cm. The inset image illustrates the splashing process and the origin of aerosols droplets. The vertical blue line placed at $K_c = 5000$ represent the threshold of the aerosols production.

If the empirical splashing parameter $K = WeOh^{-0.4}$ introduced by (Mundo et al., 1995) helps to predict the splashing rate, the mass fraction between large secondary droplets and impacting drops (Moreira et al., 2010; Okawa et al., 2022), we show in figure 11 that this parameter can also help to predict the splashing airborne rate, named here the splashing airborne release fraction S_{ARF} which is a fraction of the total secondary splashed droplet. Indeed, our experimental results for the two highest nozzle diameter (1.5 and 2 mm), the S_{ARF} can be expressed as the function of the parameter K by :

$$S_{ARF} = 2.5 \times 10^{-14} \times (K - 2667) \times (K - K_c). \tag{14}$$

[1] Notice, that in this formula, N_{lsd} does not vanish below the splashing threshold, but simply rapidly decreases for small K, in contradiction with the observation.

where K_c is the threshold value above which aerosol production is observed during our experiments. For the correlation given in equation 14, K_c correspond to the onset of aerosols droplets production with a value of about 5000. For the case of millimetric drops impact, it can be noted that this aerosolized secondary droplets production threshold value is slightly higher than the splashing threshold value, (typically between 2000 and 4000 depending on the film thickness, see for instance , (Wal et al., 2006; Cossali et al., 1997; Bai and Gosman, 1995; Yarin and Weiss, 1995). To have aerosolized secondary droplets production, it is necessary to produce the large secondary droplets first.

However, this correlation is not well adapted for the lowest nozzle radius (d_{jet} = 1mm) corresponding to very high H/d_{jet} ratio ($H/d_{jet} = 570$ here). In this type of configuration, the distance crossed by the drops resulting from the breakup of the liquid jet is large, which let the time for impacting drops to catch up and favoring simultaneous impacts of drops. This type of impact causes an interaction between the crown of the splash of different impacting drops and the coalescence of droplets from the splash, see figure 12. We suspect this effect to explain the variation of the S_{ARF} for the small nozzle from the other large nozzle, so that the splash parameter seems to be well adapted only for the case of successive and not when simultaneous impacts of drops are present.

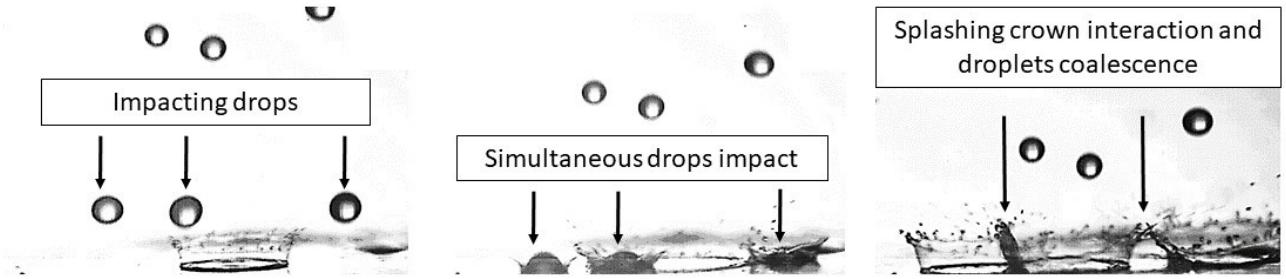

Figure 12: Simultaneous drops impact and interactions between the splashing crown. $d = 1\ mm$; $H_{imp} = 57\ cm$; $H_{imp}/d_{jet} = 570$; $V_{imp} = 3\ m{\cdot}s^{-1}$.

Finally, it is important to discuss whether the substrate properties might play a role in the aerosol production. For drop impact on a dry solid substrate, the surface properties play a crucial role in the splashing dynamics, and thus probably in the aerosol production, in particular through its roughness and wetting properties. In our case, the nature of the solid surface evolves rapidly due to the wetting from the impacting drops as a consequence of the liquid jet fragmentation. For instance, for a 2 mm liquid jet diameter, more than 10^5 drops impinge the impact surface. Therefore, even though at the beginning of the impact the surface is dry and smooth, after 10 drops impact (around 0.02 s), the impact surface is already wet at impact and recovered by a thin liquid film. There, the liquid film thickness can influence the splashing but according to the study of (Burzynski, 2021; Motzkus et al., 2011; Okawa et al., 2006) the thickness of this thin liquid film does not have a significant influence on the total amount of splashed liquid. Therefore, although the state of the impacted surface (roughness, porosity, or wettability etc) may influence the aerosol droplets generation at short time, we can neglect at first approximation its influence in our experiments.

5.3. Mass size distribution of aerosolized secondary droplets

Figure 13 shows the aerosolized secondary droplets mass distribution $dM/dlog(d_p)$ as a function of the aerosol diameter d_p for each jet diameter and for impact velocities in the range of $3.5 < v_{imp}$ $(\mathrm{m{\cdot}s^{-1}}) < 7.5$. In the representation $dM/dlog(d_p)$, the size distribution can

be approximated unimodal for the three liquid jet diameters. The aerodynamic mass median diameter of collected droplets, noted here d_{amm}, is equal to $\mathcal{O}$ $(7\,\mu m)$. The amplitude of the distribution increases with the velocity, which is consistent with the observation of increasing S_{ARF} with the impacing velocity. Moreover, the diameter of the liquid jet does not change at first sight the shape of the mass size distribution. More precisely, we can underline for the jet diameters of 1 and 1.5 mm the beginning of the appearance of another aerosol population around $10\,\mu m$, for large impact velocities (figure 13 top left) and top right)). As explained earlier, the multiple impacts lead to interaction between splashed corolla that could eventually generate either larger droplets (Roisman et al., 2002) or coalescences of aerosolized secondary droplets. Finally, we suggest that this additional aerosol population around $10\,\mu m$ might be related to the difference of the S_{ARF} observed for the 1 mm jet diameter at higher velocity.

To characterize the effects of the jet velocity on the shape of the mass size distribution, the mass distribution is normalized with the total mass of aerosols produced on figure 14. Firstly, it shows that for a given liquid jet diameter, the increase of the impact velocity does not really change the shape of the distribution and the aerodynamic mass median diameter of the aerosols produced is not shifted to the left as in the case of atomized liquid jets ((Reitz and Bracco, 1986)). This result indicates that, in this range of impact velocity, the mechanism of aerosols production is the same and therefore, the distribution of the produced aerosols can be fitted by the same log-normal distribution, defined by the following equation 15:

$$f(d_p) = \frac{dM}{M_0\ dlog(d_p)} = \frac{1}{d_p\ log(\sigma_g)\ \sqrt{2\pi}} \times \exp\Big(-\frac{(ln(d_p) - ln(d_{amm}))^2}{2\ ln(\sigma_g)^2}\Big) \tag{15}$$

with d_p the aerodynamic diameter of particles/aerosols, d_{amm} the aerodynamic mass median diameter of particles/aerosols and σ_g the geometric standard deviation of the distribution. This distribution function, line plotted in figure 14, is often used to describe size distribution of the large secondary droplets from the impact of a drop (Moreira et al., 2010). The summary of the parameters of the lognormal distribution for each liquid jet diameter is given in table 2.

Table 2: lognormal parameters.

d_{jet} (mm)	d_{amm} (μm)	σ_g (-)
1.0	7.5	1,2
1.5	6.7	1.3
2.0	6.8	1.4

We observe that the parameters of the mass distribution does only slightly vary as the nozzle diameter varies. This is evidenced by the bottom right curve of figure 14 which collapses on the same normalized mass distribution curves for the three different nozzle diameters and all the velocities available, showing very little variations between the curves.

For the three liquid jet diameters, the aerodynamic mass median diameter of the aerosolized secondary produced does not change much and can be taken equal to $\mathcal{O}(7\mu m)$. This size of aerosol is in the range of respirable aerosols.

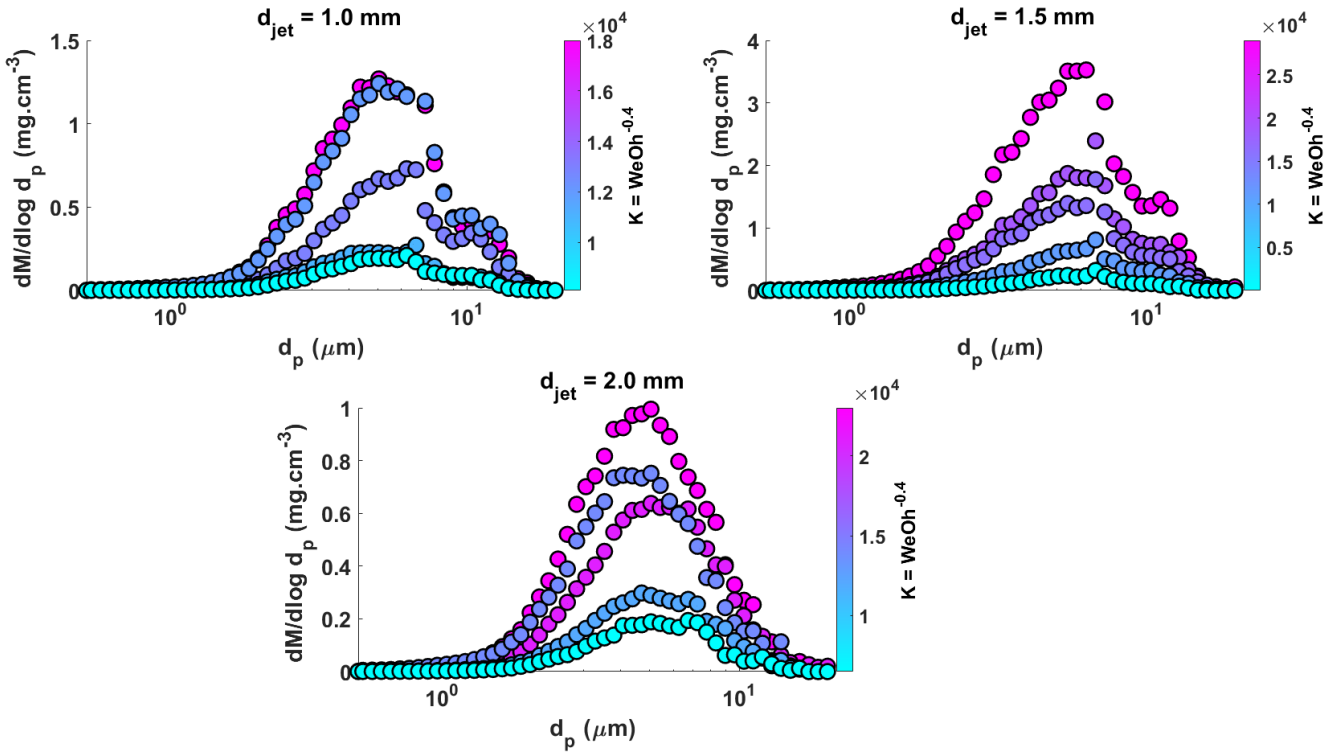

Figure 13: Aerosolized secondary droplets mass size distribution as a function of aerosol droplets diameter for different values of the splashing number $K = We \times Oh^{-0.4}$ (color map). top left) $d_{jet} = 1mm$, top right) $d_{jet} = 1.5mm$, bottom) $d_{jet} = 2mm$.

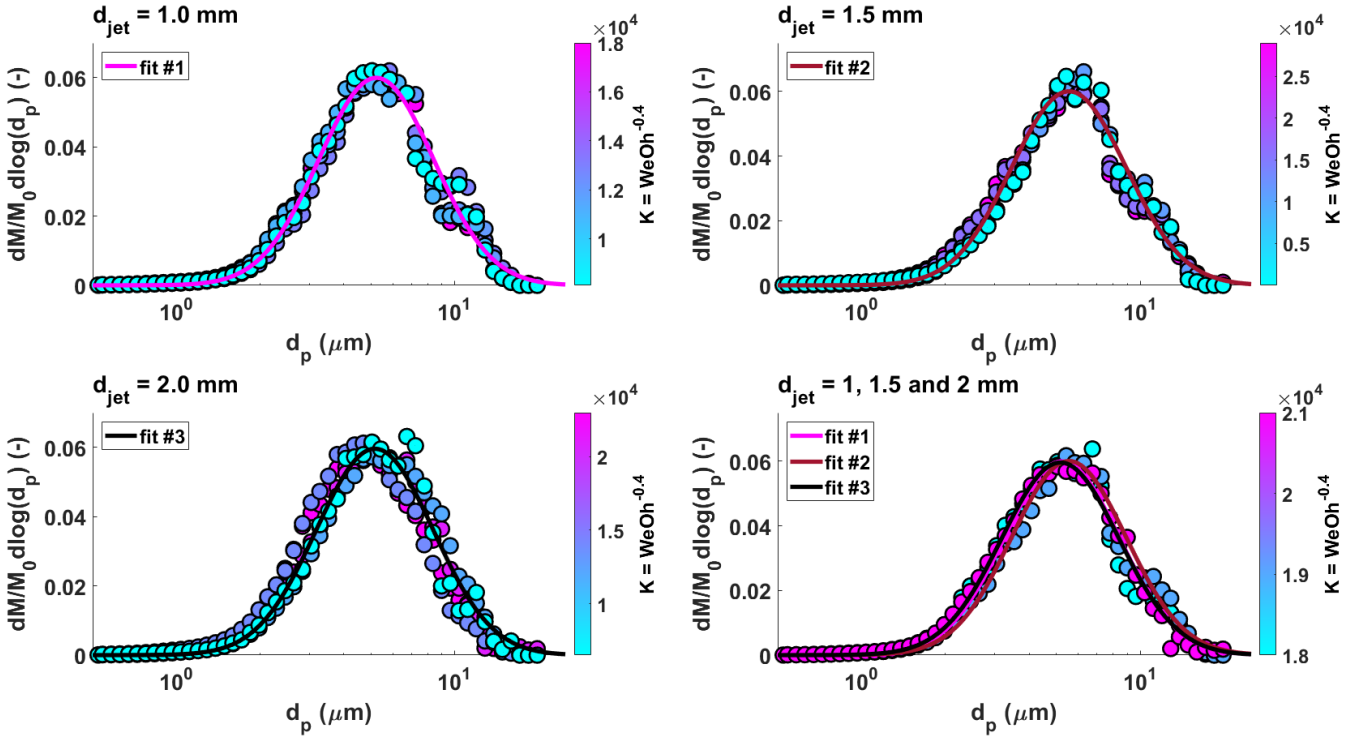

Figure 14: Normalization of aerosolized secondary droplets mass size distribution with the total mass collected on the APS M_0 as a function of aerosols droplets diameter for different values of the splashing parameter $K = WeOh^{-0.4}$ (color map). The mass size distribution is fitted with a lognormal distribution, fit 1, 2 and 3. top left) $d_{jet} = 1mm$, top right) $d_{jet} = 1.5mm$, bottom left) $d_{jet} = 2mm$ and bottom right) comparison of the three liquid jet diameters.

In addition, in nuclear buildings and plants, the transfer of these aerosols droplets within ventilation ducts can lead to local accumulation of radioactive material by aerosols deposition in ducts, implying a radiological risk during maintenance operations ((Malet et al., 2022)). This droplets aerosols can also damage the filter media in the ventilation systems and cause a loss of tightness of the radioactive containment barrier ((Lecoq et al., 2022)).

5.4. Quantifying the aerosols production rate with mass of collected aerosols

Now that we have identified that aerosol production is linked to the splash of impacting drop, we will try to quantify here how many aerosol droplets are released by each drop impact, by comparaison to the total large secondary splashed droplets.

The total number of aerosolized secondary droplets produced by each drop impact will be deduced here, from, a) the volume median diameter of the aerosols droplets produced before evaporation and collection, b) the volume corresponding to the mass of total aerosols droplets collected on the filter and c) the number of impacting drops. The impacting liquid is composed of 2.5 liter of pure water, 0.4 g/L of sodium fluorescein and 199 g/L of NaCl, corresponding to a mass fraction of NaCl of 0.166. The relative humidity (RH) inside of the enclosure is between 70 and 90%. In the case of high RH, the equilibrium size of the salt solution droplet in the humid air is rapidly reached (Rovelli et al., 2016). In order to determine the initial size of the aerosolized secondary droplets (before evaporation), we need to characterize the water activity and the density of the NaCl-droplet as the RH varies (Kreidenweis et al., 2005). We can in fact calculate the water activity of aerosols droplets from the thermodynamic Extended Aerosol Inorganics Model (E-AIM) described by (Clegg et al., 1998), accessible online [2]. The initial NaCl mass fraction is simply:

$$mfs_i = \frac{m_{NaCl}}{m_{NaCl} + m_{Water}} = \frac{m_{NaCl}}{\rho_{sol} \times V_{sol}} \tag{16}$$

where m_{NaCl}, m_{Water}, ρ_{sol} and V_{sol} are the mass of NaCl and water on the solution, the density and the volume of the solution respectively. With an initial mass fraction of NaCl of 0.166 (before evaporation), the water activity at the time where the particles are collected on the APS can be read on the figure 15.

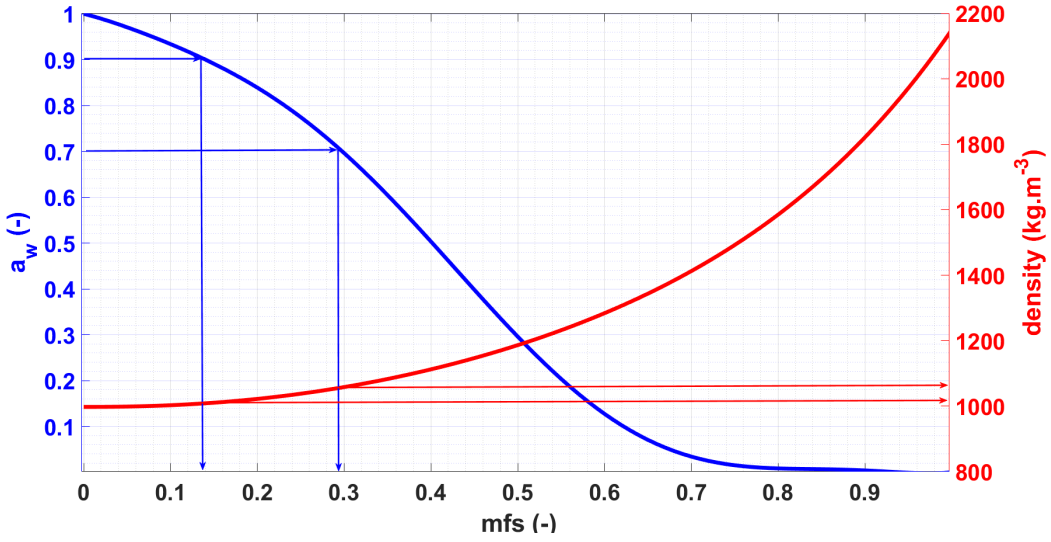

Figure 15: Curve from EAIM model. Blue line: water activity vs mfs, the mass fraction of NaCl. Red line: density vs the mass fraction of NaCl. Arrows refer to the densities corresponding to 70% and 90% of relative humidity.

[2] AIM website `http://www.aim.env.uea.ac.uk`)

The stationary droplets size is reached when the water activity, a_w , of the aerosols droplets is equal to the relative humidity inside of the enclosure which varies between 70% and 90%. In this case, the final mfs of NaCl inside of particle is equal to :

$$mfs_f = \frac{m_{N_{NaCl}}}{\rho_{part} \times V_{part}} \tag{17}$$

By dividing the equation 16 by 17 we obtain :

$$d_d = \Big(\frac{msf_f}{msf_i} \times \frac{\rho_{part}}{\rho_{sol}}\Big)^{1/3} \times d_{amm} = G.F \times d_{amm} \tag{18}$$

where G.F is the growth factor. In the relative humidity range of our experiments $[70; 90]\%$, the mass fraction and the density of NaCl particle vary in the range of $[0.14; 0.29]$, and $[1058; 1108]$ $kg.m^{-3}$ after evaporation. For these ranges of values, the growth factor between the measured and emitted droplets varies between $[1.01; 1.21]$ only, corresponding thus to a maximum radius decrease of 20%.

Therefore, with such small variation between the measured aerodynamic diameter and the initial droplet, we can consider as a first approximation that the typical initial diameter of the droplets that are aerosolized in our experiments, is $d_{amm} = 7\,\mu$m, corresponding to a volume:

$$V_d^{asd} = \Big(\frac{\pi \times d_{amm}^3}{6}\Big). \tag{19}$$

Thus the total number of aerosolized droplet can be estimated following;

$$N_t^{asd} = \frac{V_L \times S_{ARF}}{V_d^{asd}} \tag{20}$$

On the other hand the total number of impacting droplets can be estimated by considering the diameter of the impacting drop following eq. 6:

$$N_{drops} = \frac{V_L}{V_{drop}} = \frac{6 \times V_L}{\pi \times 1.89 \times d_j^3} \tag{21}$$

Finally, we can calculate the number of aerosolized secondary droplets produced per drop impact N_i^{asd} as:

$$N_i^{asd} = \frac{N_t^{asd}}{N_{drops}} = S_{ARF}\frac{V_{drop}}{V_d^{asd}} = S_{ARF} \times 1.89\Big(\frac{d_j}{d_{amm}}\Big)^3 \tag{22}$$

We find in this study, in the range of Weber number $\mathcal{O}(10^2 - 10^3)$, that the number of aerosolized secondary droplets produced per drop impact is around $\mathcal{O}(6 - 3.5 \times 10^2)$, as shown figure 16.

It is interesting to compare this number with the typical number of large secondary droplets produced by the impact of a drop, as discussed by (Okawa et al., 2021). For the same Weber number range, these data are superimposed (red stars) on the figure 16, showing a a similar evolution as the weber number increases. However, the number of aerosolized secondary droplets seems to be $\mathcal{O}(5)$ times smaller than the number of large secondary droplets, indicating that most of these droplets do not transform into aerosols!

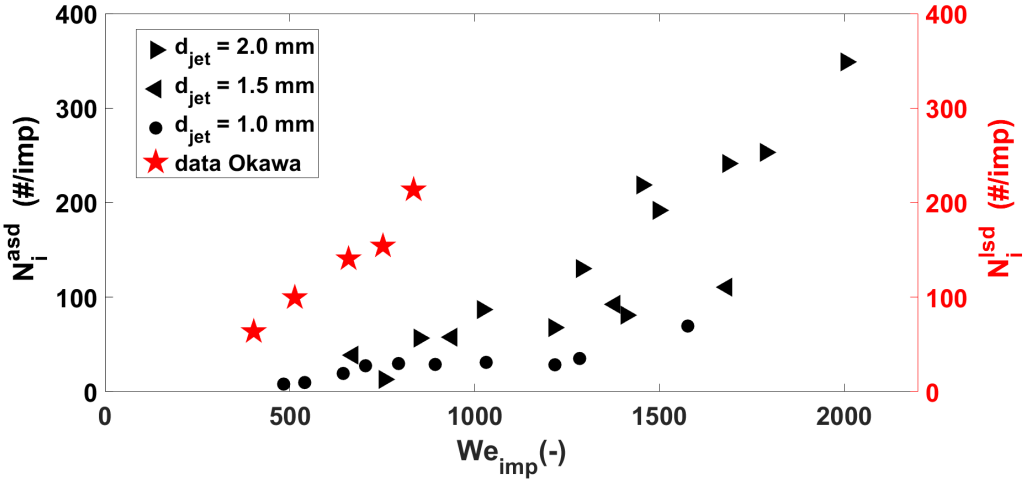

Figure 16: Comparison between the aerosolized secondary droplets and large secondary droplets during the impact of a drop. Black symbols: aerosolized secondary droplets number obtained from the mass of total aerosols collected on the filter. Red symbols: large secondary droplets number obtained from the the results of (Okawa et al., 2022). His droplets are produced with a pure water drop of 2 mm of diameter.

5.5. On the origin of the aerosols

If we have proven above that aerosol production is directly linked to the splashing of the drop at impact, we need to elucidate which of these secondary droplets contribute to the S_{ARF}. Indeed, splashed droplets may have different origins, from tiny droplets ejected almost horizontally at early times in the so-called prompt splash (not observed in our experiments) to *a priori* larger ones coming from the destabilization of the liquid lamella in corolla splashes (Marcotte et al., 2019). We can estimate the diameter of the micro-droplets produced by the prompt splash is around 5 μm and are 1/1000 smaller than the the original impact drops (Thoroddsen et al., 2012). However, large droplets are formed by the instability of the corolla, due to the combination of both Rayleigh-Taylor and Rayleigh-Plateau instabilities of the rim located at the edge of the corolla (Roisman et al., 2006; Agbaglah et al., 2013). Fingers are then formed from which large droplets break-up, accompanied by small satellite droplets on the one hand but leading also to the rupture of the rim corolla in small droplets on the other hand. This global mechanism is illustrated on figure 17. Recall that we have shown that only droplets at least below 20 μm of diameter can lead to an aerosol. By contrast, we identify here that the satellite droplets do correspond by size to the aerosol detected, suggesting that if the crucial mechanism for aerosol production is related to the splashing, the aerosols are not coming directly from the larger drops detached but from the small satellite ones generated by the drop break-up and the fragmentation of the liquid fingers. These tiny droplets have not been widely studied in the literature because they have a very low mass compared to the larger droplets directly detached from the rim and therefore do not contribute much to the industrial process. Here we suggest that they are predominant for air contamination.

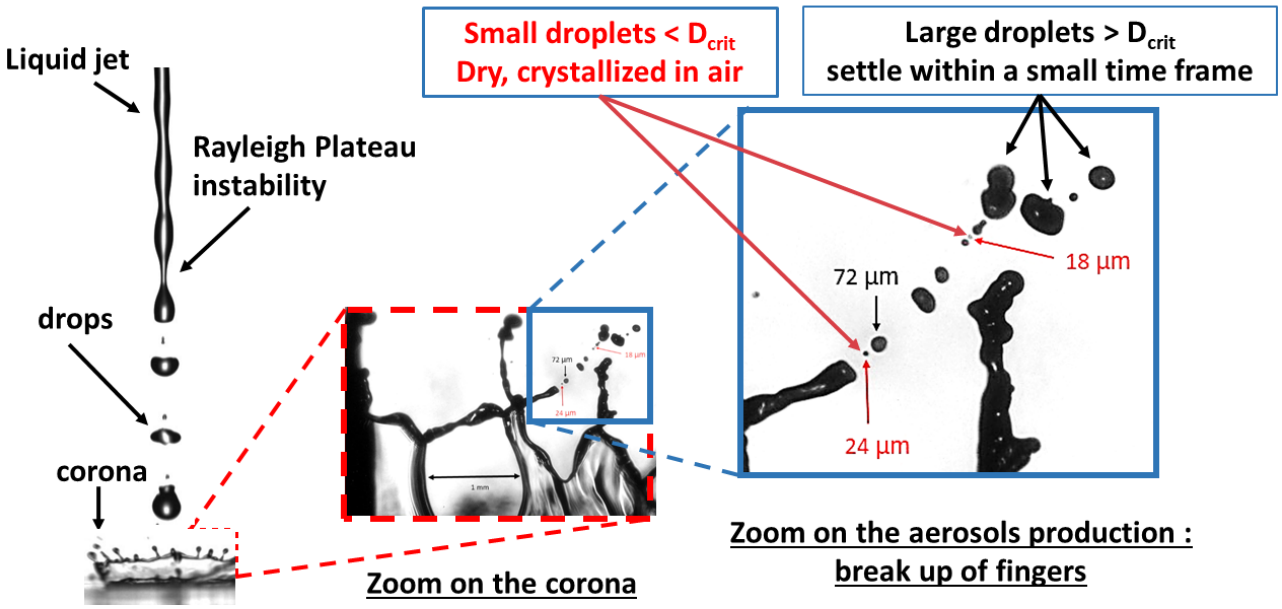

Figure 17: Identification of one of the mechanism leading to the droplets aerosols production. Left image) Break up of a impacting liquid jet; middle image) zoom on the splashing zone produced by splashing process ; right image) zoom on the "corona" and the break up of the fingers.

5.6. Conclusion and perspectives

We have characterized the aerosol production for a liquid jet impacting a solid plate when varying both the jet diameter and impact velocity, corresponding to variations of the dimensionless numbers: Re $\sim \mathcal{O}(10^3 - 10^4)$, We $\sim \mathcal{O}(10^2 - 10^3)$, K $\sim \mathcal{O}(10^3 - 10^4)$. The main results of our study are summarized below:

1. The DICAPRIO experimental device developed at IRSN is well configured to characterize accurately, the aerosolized secondary droplets during the impact of a liquid jet or a series of drops. Our experimental study pointed out for the first time, to our knowledge, the airborne release fraction from the splashed secondary droplets produced by a liquid jet impingement.
2. For the droplets generation, the shape of the impacting liquid is an important parameter. At equal impacting velocity: the total amount of aerosolized secondary droplets produced by a smooth jet is almost zero, for a rough impacting jet (turbulence or surface waves) the aerosolized secondary droplets starts to appear by puff whereas for the case of series of impacting drops, the aerosolized secondary droplets produced are systematic and more important than the two last cases.
3. From the mass distribution, the study has shown that the mass droplets size distribution is independent of the impact conditions studied in terms of impacting droplet diameter and impact velocity. For all configurations, the aerodynamic mass diameter is around $\mathcal{O}(7\ \mu m)$ and the standard deviation is around $\mathcal{O}(1.3)$. The distribution can also be fitted with a log-normal distribution. Considering the relative humidity values inside DICAPRIO, and the measured techniques, this diameter corresponds roughly to the typical radius of the emitted droplets.
4. The splashing parameter K, derived from theoretical, experimental and numerical studies, used in the literature to determine the splashing threshold for drop impact and often used to quantify the splashed mass ratio, was used in this study to model the splashing airborne release fraction (mass ratio of aerosolized secondary droplets). It was shown that K can be used to predict the splashing airborne release fraction if the ratio between the impact

height and the impacting drop diameter H/d is not high, H/d $<$ 380. For values of H/d $>$ 380 we could not correlate our experimental results probably due to the fact that in these configurations, simultaneous drop impacts have to be considered, which cause corolla interactions or/and coalescence of aerosolized droplets in particular.

5. The number of aerosolized secondary droplets per drop impact has been estimated as a function of the splashing parameter: it increases with the Weber number as the number of droplets splashed although it is about one fifth (Okawa et al., 2022).
6. We suggest that the aerosolized secondary droplets that we measure come from the destabilization of the liquid lamella in corolla splashes. More precisely, the radius of these droplets are of the same order than that of the satellites droplets formed during the break up of the fingers formed at the rim of the corolla.
7. The empirical relation given here for the prediction of the splashing airborne fraction and the number of aerosolized secondary droplets per drop impact can be used to calculated various statistics on secondary droplets. For air contamination, those relations can be also used by the nuclear authority safety in the case of an accident leak of radioactive liquid. This study provides thus a complementary methodology for the quantification of the total amount of secondary droplets produced by drop impact by using both the physics of aerosols and fluid dynamics.

References

References

Agbaglah, G., Josserand, C., Zaleski, S., 2013. Longitudinal instability of a liquid rim. Phys. Fluids 25, 022103.

Allen, A., Hughes, P., 1984. The rayleigh–taylor instability in astrophysical fluids. Monthly Notices of the Royal Astronomical Society 208, 609–621.

Bai, C., Gosman, A., 1995. Development of methodology for spray impingement simulation. SAE transactions , 550–568.

Balachandar, S., Zaleski, S., Soldati, A., Ahmadi, G., Bourouiba, L., 2020. Host-to-host airborne transmission as a multiphase flow problem for science-based social distance guidelines. International Journal of Multiphase Flow 132, 103439. URL: https://doi.org/10.1016/j.ijmultiphaseflow.2020.103439, doi:10.1016/j.ijmultiphaseflow.2020.103439, arXiv:2008.06113.

Baron, P.A., Willeke, K., 2001. Aerosol measurement: principles, techniques, and applications .

Bergeron, V., Bonn, D., Martin, J.Y., Vovelle, L., 2000. Indoor air quality for chemical and ultrafine particle contaminants from printers. Nature 405, 772–775.

Bohr, T., Ellegaard, C., Hansen, A.E., Haaning, A., 1996. Hydraulic jumps, flow separation and wave breaking: An experimental study. Physica B: Condensed Matter 228, 1–10. URL: http://dx.doi.org/10.1016/S0921-4526(96)00373-0, doi:10.1016/S0921-4526(96)00373-0.

Bourouiba, L., 2021. Fluid dynamics of respiratory infectious diseases .

Breitenbach, J., Roisman, I.V., Tropea, C., 2018. From drop impact physics to spray cooling models: a critical review. Experiments in Fluids 59, 1–21. URL: http://dx.doi.org/10.1007/s00348-018-2514-3, doi:10.1007/s00348-018-2514-3.

Burzynski, D., 2021. On the Impact of High-Speed Drops on Dry and Wetted Surfaces. Ph.D. thesis.

Clegg, S.L., Brimblecombe, P., Wexler, A.S., 1998. Thermodynamic model of the system h+- nh4+- so42– no3– h2o at tropospheric temperatures. The Journal of Physical Chemistry A 102, 2137–2154.

Cossali, G.E., Coghe, A., Marengo, M., 1997. The impact of a single drop on a wetted solid surface. Experiments in fluids 22, 463–472.

Dumouchel, C., 2008. On the experimental investigation on primary atomization of liquid streams. Experiments in Fluids 45, 371–422. doi:10.1007/s00348-008-0526-0.

Eggers, J., Villermaux, E., 2008. Physics of liquid jets. Reports on Progress in Physics 71. doi:10.1088/0034-4885/71/3/036601.

Errico, 1986. A study of the interaction of liquid jets with solid surfaces. Preventing School Failure 51, 49–51.

Josserand, C., Ray, P., Zaleski, S., 2016. Droplet impact on a thin liquid film: anatomy of the splash. Journal of Fluid Mechanics 802, 775–805.

Josserand, C., Thoroddsen, S., 2016. Drop impact on a solid surface. Annual Rev. Fluid Mech. 48, 365–391.

Josserand, C., Zaleski, S., 2003. Droplet splashing on a thin liquid film. Physics of fluids 15, 1650–1657.

Kreidenweis, S., Koehler, K., DeMott, P., Prenni, A., Carrico, C., Ervens, B., 2005. Water activity and activation diameters from hygroscopicity data-part i: Theory and application to inorganic salts. Atmospheric Chemistry and Physics 5, 1357–1370.

Lecoq, M., Bourrous, S., Thomas, D., Appert-Collin, J.C., Floc'Hlay, F., Barrault, M., 2022. Investigation of the possibility of application of metal fibrous media in the process of filtration of liquid aerosols. Atmosphere 13, 1633.

Leroux, S., Dumouchel, C., Ledoux, M., 1996. The stability curve of newtonian liquid jets. Atomization and Sprays 6, 623–647. doi:10.1615/AtomizSpr.v6.i6.10.

Lienhard, J., Liu, X., Gabour, L., 1992. Splattering and heat transfer during impingement of a turbulent liquid jet .

Lindsley, W.G., Pearce, T.A., Hudnall, J.B., Davis, K.A., Davis, S.M., Fisher, M.A., Khakoo, R., Palmer, J.E., Clark, K.E., Celik, I., et al., 2012. Quantity and size distribution of cough-generated aerosol particles produced by influenza patients during and after illness. Journal of occupational and environmental hygiene 9, 443–449.

Malet, J., Radosavljevic, M., Mbaye, M., Costa, D., Wiese, J., Gehin, E., 2022. Flow characterization of various singularities in a real-scale ventilation network with rectangular ducts. Building and Environment , 109223.

Marcotte, F., Michon, G.J., Séon, T., Josserand, C., 2019. Droplet impact on a thin liquid film: anatomy of the splash. Phys. Rev. Lett. 122, 014501.

Moreira, A.L.N., Moita, A.S., Panão, M.R., 2010. Advances and challenges in explaining fuel spray impingement: How much of single droplet impact research is useful? Progress in Energy and Combustion Science 36, 554–580. doi:10.1016/j.pecs.2010.01.002.

Motzkus, C., Gensdarmes, F., Géhin, E., 2009. Parameter study of microdroplet formation by impact of millimetre-size droplets onto a liquid film. Journal of Aerosol Science 40, 680–692. URL: http://dx.doi.org/10.1016/j.jaerosci.2009.04.001, doi:10.1016/j.jaerosci.2009.04.001.

Motzkus, C., Gensdarmes, F., Géhin, E., 2011. Study of the coalescence/splash threshold of droplet impact on liquid films and its relevance in assessing airborne particle release. Journal of Colloid and Interface Science 362, 540–552. URL: http://dx.doi.org/10.1016/j.jcis.2011.06.031, doi:10.1016/j.jcis.2011.06.031.

Mundo, C., Sommerfeld, M., Tropea, C., 1995. Droplet-wall collisions: Experimental studies of the deformation and breakup process. International Journal of Multiphase Flow 21, 151–173. doi:10.1016/0301-9322(94)00069-V.

Okawa, T., Kawai, K., Kubo, K., Kitabayashi, S., 2022. Fundamental characteristics of secondary drops produced by early splash during single-drop impingement onto a thick liquid film. Experimental Thermal and Fluid Science 131, 110533. URL: https://doi.org/10.1016/j.expthermflusci.2021.110533, doi:10.1016/j.expthermflusci.2021.110533.

Okawa, T., Kubo, K., Kawai, K., Kitabayashi, S., 2021. Experiments on splashing thresholds during single-drop impact onto a quiescent liquid film. Experimental Thermal and Fluid Science 121, 110279. URL: https://doi.org/10.1016/j.expthermflusci.2020.110279, doi:10.1016/j.expthermflusci.2020.110279.

Okawa, T., Shiraishi, T., Mori, T., 2006. Production of secondary drops during the single water drop impact onto a plane water surface. Experiments in fluids 41, 965–974.

Passandideh-Fard, M., Teymourtash, A.R., Khavari, M., 2011. Numerical study of circular hydraulic jump using volume-of-fluid method. Journal of Fluids Engineering, Transactions of the ASME 133, 1–11. doi:10.1115/1.4003307.

Rein, M., 1993. Phenomena of liquid drop impact on solid and liquid surfaces. Technical Report.

Reitz, R.D., Bracco, F.V., 1986. Mechanisms of breakup of round liquid jets. Encyclopedia of Fluid Mechanics , 233–249.

Renoux, A., Boulaud, D., 1998. Les aérosols: physique et métrologie. Tec & Doc Lavoisier.

Rioboo, R., Tropea, C., Marengo, M., 2001. Outcomes from a drop impact on solid surfaces. Atomization and sprays 11.

Roisman, I., Prunet-Foch, B., Tropea, C., Vignes-Adler, M., 2002. Multiple drop impact onto a dry solid substrate. J. Coll. Inter. Sci. 256, 396–410.

Roisman, I.V., Horvat, K., Tropea, C., 2006. Spray impact: rim transverse instability initiating fingering and splash, and description of a secondary spray. Physics of Fluids 18, 102104.

Roisman, I.V., Tropea, C., 2002. Impact of a drop onto a wetted wall: Description of crown formation and propagation. Journal of Fluid Mechanics 472, 373–397. doi:10.1017/S0022112002002434.

Rovelli, G., Miles, R.E., Reid, J.P., Clegg, S.L., 2016. Accurate measurements of aerosol hygroscopic growth over a wide range in relative humidity. The Journal of Physical Chemistry A 120, 4376–4388.

Sow, M., Leblois, Y., Gensdarmes, F., 2019. Experimental study of aerosol release following liquid leaks of fission products concentrates simulants. Nuclear Engineering and Design 341, 46–55.

Stow, C.D., Hadfield, M.G., 1981. An experimental investigation of fluid flow resulting from the impact of a water drop with an unyielding dry surface. Proceedings of the Royal Society of London. A. Mathematical and Physical Sciences 373, 419–441.

Thoroddsen, S., Etoh, T., Takehara, K., 2003. Air entrapment under an impacting drop. J. Fluid Mech. 706, 560–570.

Thoroddsen, S., Takehara, K., Etoh, T., 2012. Micro-splashing by drop impacts. J. Fluid Mech. 706, 560–570.

Trainer, D., 2016. Breakup length and liquid splatter characteristics of air-assisted water jets. International Journal of Multiphase Flow 81, 77–87. URL: http://dx.doi.org/10.1016/j.ijmultiphaseflow.2016.02.005, doi:10.1016/j.ijmultiphaseflow.2016.02.005.

Vander Wal, R.L., Berger, G.M., Mozes, S.D., 2006. The combined influence of a rough surface and thin fluid film upon the splashing threshold and splash dynamics of a droplet impacting onto them. Experiments in fluids 40, 23–32.

Vignati, E., Facchini, M., Rinaldi, M., Scannell, C., Ceburnis, D., Sciare, J., Kanakidou, M., Myriokefalitakis, S., Dentener, F., O'Dowd, C., 2010. Global scale emission and distribution of sea-spray aerosol: Sea-salt and organic enrichment. Atmospheric Environment 44, 670–677.

Wal, R.L.V., Berger, G.M., Mozes, S.D., 2006. The splash/non-splash boundary upon a dry surface and thin fluid film. Experiments in fluids 40, 53–59.

Wassenberg, J.R., Stephan, P., Gambaryan-Roisman, T., 2019. The influence of splattering on the development of the wall film after horizontal jet impingement onto a vertical wall. Experiments in Fluids 60, 1–17. URL: https://doi.org/10.1007/s00348-019-2810-6, doi:10.1007/s00348-019-2810-6.

Wilson, N., Corbett, S., Tovey, E., 2020. Airborne transmission of covid-19. bmj 370.

Wu, Z.N., 1992. Modélisation et calcul implicite multidomaine d'écoulements diphasiques gaz-gouttelettes. Ph.D. thesis. Paris 6.

Yarin, A., 2006. Drop impact dynamics: Splashing, spreading, receding, bouncing... Annual Rev. Fluid Mech. 38, 159–192.

Yarin, A.L., Weiss, D.A., 1995. Impact of Drops on Solid Surfaces: Self-Similar Capillary Waves, and Splashing as a New Type of Kinematic Discontinuity. volume 283. doi:10.1017/S0022112095002266.

Zhan, Y., Kuwata, Y., Maruyama, K., Okawa, T., Enoki, K., Aoyagi, M., Takata, T., 2020. Effects of surface tension and viscosity on liquid jet breakup. Experimental Thermal and Fluid Science 112, 109953. URL: https://doi.org/10.1016/j.expthermflusci.2019.109953, doi:10.1016/j.expthermflusci.2019.109953.